Commun. Comput. Phys.
doi: 10.4208/cicp.050413.170314a

Vol. **16**, No. 3, pp. 799-816
September 2014

A Two-Phase Flow Simulation of Discrete-Fractured Media using Mimetic Finite Difference Method

Zhaoqin Huang, Xia Yan and Jun Yao*

School of Petroleum Engineering, China University of Petroleum (East China), Qingdao 266580, P.R. China.

Received 5 April 2013; Accepted (in revised version) 17 March 2014

Available online 8 July 2014

Abstract. Various conceptual models exist for numerical simulation of fluid flow in fractured porous media, such as dual-porosity model and equivalent continuum model. As a promising model, the discrete-fracture model has been received more attention in the past decade. It can be used both as a stand-alone tool as well as for the evaluation of effective parameters for the continuum models. Various numerical methods have been applied to the discrete-fracture model, including control volume finite difference, Galerkin and mixed finite element methods. All these methods have inherent limitations in accuracy and applicabilities. In this work, we developed a new numerical scheme for the discrete-fracture model by using mimetic finite difference method. The proposed numerical model is applicable in arbitrary unstructured gridcells with full-tensor permeabilities. The matrix-fracture and fracture-fracture fluxes are calculated based on powerful features of the mimetic finite difference method, while the upstream finite volume scheme is used for the approximation of the saturation equation. Several numerical tests in 2D and 3D are carried out to demonstrate the efficiency and robustness of the proposed numerical model.

AMS subject classifications: 76S05, 65N08, 65N55, 35J25

Key words: Fractured porous media, discrete-fracture model, two-phase flow, mimetic finite difference method.

1 Introduction

In response to stress, all rocks in the earth's crust are fractured to some extent. Fractures are important in many engineering and environmental practices. They can behave as either hydraulic conductors or barriers, and occur on different scales, from microscopic to continental. These cause modeling fluid flow in fractured rock to be a challenging work.

*Corresponding author. *Email addresses:* huangzhqin@upc.edu.cn (Z. Q. Huang), jsyanxia@163.com (X. Yan), RCOGFR_UPC@126.com (J. Yao)

Since 1960s, various conceptual models have been developed, which can be classified into four broad classes: dual-porosity model and its variations, equivalent continuum model, discrete-fracture model, and hybrid model [1].

The dual-porosity concept was introduced by Barenblatt et al. [2]. In this model, there are two parallel continua, i.e. the fracture and the matrix systems, which are connecting with transfer function. Because of its computational efficiency, dual-porosity model has been widely used to simulate the fluid flow in fractured hydrocarbon reservoirs [3–7]. However, how to accurately evaluate the transfer function is still an open problem, especially for multi-phase flow [8–10]. By further subdividing individual matrix blocks, the Multiple INteraction Continua (MINC) method [11–14] have better accuracy and features than the conventional dual-porosity model.

In comparison, the equivalent continuum model (ECM) represents the fractured rock as a single-porosity continuum. The heterogeneity of fractured rocks is modeled by using effective parameters, such as equivalent permeability and effective porosity. The ECM has long been used for modeling fracture-matrix flow due to its simple data requirements and computational efficiency [14, 15]. However, the calculation of the effective parameters for multi-phase flow is still a challenge, such as relative permeabilities and capillary pressure [16]. In addition, the instantaneous equilibrium assumption for fracture-matrix systems also limits the application of the ECM approach for modeling general multi-phase flow.

As effective continuum models, either dual-porosity model or ECM is not well suited for the modeling of discrete-fractured media, in which a small number of large-scale fractures may dominate the flow. For this reason, the discrete-fracture model (DFM), which describes the fractures explicitly in the medium, are received a growing attention in the past decade. Most DFMs are based on meshing the fractures explicitly, either with an equi-dimensional formulation where fracture gridcells have the same dimension as the matrix [17–19] or with a hybrid formulation where the fractures are geometrically simplified by using $(d-1)$-dimensional gridcells in a d-dimensional domain [20–24]. An alternative approach is to deal with fractures as immersed interfaces in gridcells, including embedded-fracture model [25, 26] and non-matching grid method [27]. In the former, the fractures are embedded into a coarse structured grid and modelled through transport indices.

Limited to the present computational capacity, the DFM is only applicable to the situations where a small number of fractures dominate the fractured rock. One approach to overcome this deficiency is to combine the DFM with the continuum model, i.e. the hybrid model [1, 14, 28]. While large-scale fractures are represented as discrete elements explicitly, small-scale fractures are included as effective parameters in building continuum approximations [25, 29]. As the effective permeability are generally full-tensor, an efficient numerical scheme handling anisotropy in the permeability and discrete fractures is necessary. Various numerical methods based on DFM have been used to simulate fluid flow in discrete-fractured media, including the finite difference (FD) [30, 31], finite volume (FV) [32–35], Galerkin finite element (GFE) [21, 36], and mixed finite element

(MFE) [23] methods. Herein, our emphasis is on FV and MFE methods due to their good local conservativeness.

Karimi-Fard et al. [34] introduced a simplified cell-centered FV method for two-phase flow in fractured media by using two-point flux approximation (TPFA). Recently, Sandve et al. [35] provided a consistent discretization for anisotropic permeabilities using a multi-point flux approximation (MPFA). In order to handle the multiple intersecting fractures, they have used the star-delta transformation to evaluate the transmissibility between the intersecting fractures. The authors, however, mentioned that the star-delta transformation is just an approximation for two-phase flow problems. Hoteit and Firoozabadi [23] developed an efficient numerical model for two-phase flow in fractured media using MFE method, in which the treatment with multiple intersecting fractures in a natural and accurate way. Unfortunately, the MFE scheme results in an algebraic saddle point problem. One possible solution is to use the mixed-hybrid formulation [37–39]. However, the construction of the basis functions for MFE is a non-trivial task for general polyhedral meshes. Recently, Brezzi et al. [40,41] developed the mimetic finite difference (MFD) method whose formulation is similar to the mixed-hybrid formulation. But the MFD approaches the discretization in a more easier way for general grids than MFE [39,42].

In this work, we developed an efficient DFM valid for anisotropic permeabilities by using MFD method. First, we assume that an effective permeability tensor exists for the matrix system which contains small-scale fractures, and focus on the MFD discretization of DFM. The organization of this paper is as follows. In Section 2, we present the model equations which are valid in fractures and matrix, simultaneously the geometrical discretization of the discrete-fracture model is described. Then the MFD discretization for DFM is described in detail in Section 3. In Section 4, the upstream-weighting FV discretization for the saturation equation is used since it is used almost exclusively in commercial simulators. Some numerical examples are shown in Section 5 and several remarks are concluded in Section 6.

2 Model equations and geometrical discretization

2.1 Model equations

We consider the flow of two immiscible and incompressible phases (wetting and non-wetting) and assume no-flow boundary conditions. The flow equations can then be formulated as an elliptic equation for the globe pressure p and the total Darcy velocity $\boldsymbol{v}$ (the details can be found in [43]),

$$\boldsymbol{v}=-\boldsymbol{K}\lambda\cdot\nabla p+\boldsymbol{K}\cdot(\lambda_{\rm w}\rho_{\rm w}+\lambda_{\rm n}\rho_{\rm n})\boldsymbol{G},\quad \nabla\cdot\boldsymbol{v}=q. \tag{2.1}$$

Here, q is a source term representing injection and production wells, $\boldsymbol{K}$ is the effective permeability tensor, and $\lambda=\lambda_{\rm n}+\lambda_{\rm w}$ denotes the total mobility. The mobility of phase is given by $\lambda_l=k_{{\rm r}l}/\mu_l$, where μ_l is viscosity of phase l and $k_{{\rm r}l}(S_{\rm w})$ is the relative permeability. $\boldsymbol{G}=-g\nabla z$ is the gravitational pull-down force, where g is the gravitational constant

and z is the spatial coordinate in the upward vertical direction. The second primary unknown is the wetting phase saturation S_w, which denotes the volume fraction of water and is described by the transport equation

$$\phi\frac{\partial S_w}{\partial t}+\nabla\cdot\boldsymbol{v}_w=q_w, \tag{2.2}$$

$$\boldsymbol{v}_w=f_w[\boldsymbol{v}+\boldsymbol{K}\lambda_n\cdot\nabla p_{cnw}+\boldsymbol{K}\lambda_n\cdot(\rho_w-\rho_n)\boldsymbol{G}], \tag{2.3}$$

where ϕ is the porosity, $f_w=\lambda_w/\lambda$ is the fractional flow function, $p_{cnw}=p_n-p_w$ is the capillary pressure, and $\nabla p_{cnw}=\frac{\partial p_{cnw}}{\partial S_w}\nabla S_w$.

The system of Eqs. (2.1)-(2.3) are valid for matrix and fractures. In this work, we will use an IMPES (IMplicit Pressure and Explicit Saturation solver) sequential splitting scheme to solve the flow equations, i.e., the pressure equation is solved at the current time-step using saturation values from the previous time-step, then the total velocity $\boldsymbol{v}$ is kept constant as a parameter in Eq. (2.2), while the saturation is advanced in time.

2.2 Geometrical discretization

In this work, an unstructured geometrical discretization based on control-volume partitioning is used to adapt the complexity of fractures. As mentioned in Section 1, the fractures gridcells are geometrically simplified by dimension reduction method, i.e. using $(d-1)$-dimensional gridcells in a d-dimensional domain. In a 2D domain, the fractures are represented by the matrix gridcell segments, which are 1D geometry entities as illustrated in Fig. 1. This simplification removes the length-scale contrast caused by the explicit representation of the fracture aperture as in the equi-dimensional DFM. As a result, computational efficiency is improved considerably. The fractures aperture are just considered in the computational domain. For this reason, the DFM can only handle a limited number of fractures (of the order of thousands) for consideration of computational resources.

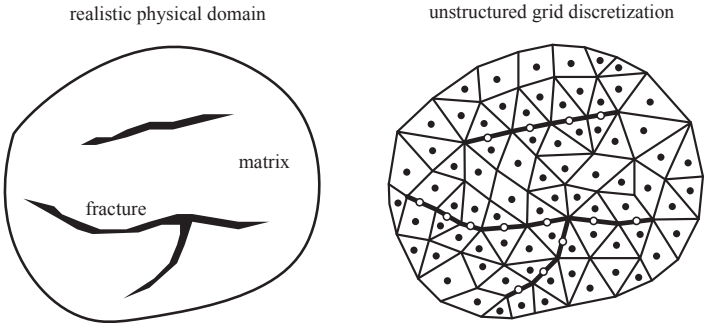

Figure 1: Schematic of a discrete-fractured medium (left) and the corresponding unstructured gridding (right), where the thick segments represent the fracture gridcells.

Here, we used a free Delaunay triangulation algorithm (EasyMesh) for 2D problems. More details of EasyMesh can be found in [44]. And the opensource C++ program (TetGen) will be used for gridding the 3D discrete-fracture model. For a 3D domain, defined by its boundary (such as a fracture surface), TetGen generates the boundary constrained (Delaunay) tetrahedralization. The interested readers is referred to [45] for more details. However, the gridding of complex fractured geological models is still a challenging issue. We plan to address this important issue as our future work.

3 Discretization of the pressure equation

In this section, we start by discussing the mimetic discretizations in matrix and fractures using the inner product concept, which can be used to design the properties of the MFD method. Here, only a short description of the MFD method will be given. The interested reader is referred to [39] and [42] for more details. Then, we will discuss the MFD numerical scheme for DFM in more detail.

3.1 Mimetic discretization method

The MFD method (see [40]) is defined in terms of a local inner product $\boldsymbol{M}_i$ in a gridcell, which gives the gridcell-based discretisation of Darcy's law

$$\boldsymbol{M}_i \boldsymbol{v}_i = \boldsymbol{e}_i p_i - \boldsymbol{\pi}_i. \tag{3.1}$$

Here, $\boldsymbol{e}_i = (1,\cdots,1)^{\mathrm{T}}$, $\boldsymbol{\pi}$ is the pressure at the face centroids and p the gridcell pressure at the gridcell centroid as depicted in Fig. 2. The MFD method is constructed so that they are exact for linear pressure fields and give a symmetric positive-definite matrix $\boldsymbol{M}_i$. A linear pressure field can be written in the form $p = \boldsymbol{a}\cdot\boldsymbol{x} + b$ for a constant vector $\boldsymbol{a}$ and scalar b, giving a Darcy velocity $\boldsymbol{v} = -\boldsymbol{K}\cdot\boldsymbol{a}$. Let $\boldsymbol{n}_k$ denote the area-weighted normal vector to face number k and $\boldsymbol{x}_{ik}$ be the vector pointing from the gridcell centroid to the face centroid. Then the flux and pressure drop are given by

$$v_{ik} = -\boldsymbol{n}_{ik}\cdot\boldsymbol{K}\cdot\boldsymbol{a}, \quad p_i - \pi_k = \boldsymbol{x}_{ik}\cdot\boldsymbol{a}. \tag{3.2}$$

Substituting Eq. (3.2) into Eq. (3.1), we see that the matrices $\boldsymbol{M}$ satisfies the following consistency conditions

$$\boldsymbol{M}_i\boldsymbol{N}_i\boldsymbol{K}_i = \boldsymbol{X}_i, \quad \boldsymbol{N}_i = \begin{bmatrix} \boldsymbol{n}_{i1} \\ \vdots \\ \boldsymbol{n}_{im} \end{bmatrix}, \quad \boldsymbol{X}_i = \begin{bmatrix} \boldsymbol{x}_{i1} \\ \vdots \\ \boldsymbol{x}_{im} \end{bmatrix}, \tag{3.3}$$

where m is the number of faces within gridcell Ω_i. By augmenting Eq. (3.3) with flux and pressure continuity across gridcell faces, we can obtain the following linear system

$$\begin{bmatrix} \boldsymbol{B} & -\boldsymbol{C} & \boldsymbol{D} \\ \boldsymbol{C}^{\mathrm{T}} & 0 & 0 \\ \boldsymbol{D}^{\mathrm{T}} & 0 & 0 \end{bmatrix} \begin{bmatrix} \boldsymbol{v} \\ \boldsymbol{p} \\ \boldsymbol{\pi} \end{bmatrix} = \begin{bmatrix} \boldsymbol{g} \\ \boldsymbol{q} \\ \boldsymbol{f} \end{bmatrix}, \tag{3.4}$$

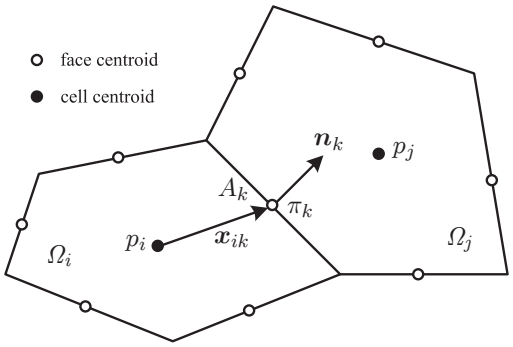

Figure 2: Schematic of grid analysis used to define the mimetic inner product.

Here, the first row corresponds to Darcy's law in the form (3.1), the second row represents the mass conservation for each gridcell, while the third row expresses the flux continuity of gridcell faces.

Therefore, $\boldsymbol{v}$ denotes the outward face fluxes ordered cell-wise (fluxes over interior faces and fractures appear twice), $\boldsymbol{p}$ denotes the cell pressures and $\boldsymbol{\pi}$ the face pressures. The matrices $\boldsymbol{B}$ and $\boldsymbol{C}$ are block diagonal with each block corresponding to a gridcell. For the two matrices, the i-th blocks are given as $\boldsymbol{M}_i$ and $\boldsymbol{e}_i$, respectively. Similarly, each column of $\boldsymbol{D}$ corresponds to a unique face and has one (for boundary faces) or two (for interior faces) unit entries corresponding to the index(s) of the face in the cell-wise ordering. In the right-hand side, $\boldsymbol{g}$ is the gravity effects, $\boldsymbol{q}$ is the source/sink terms, and $\boldsymbol{f}$ is the Neumann boundary conditions. For simplicity, we will set $\boldsymbol{f}=0$ by considering the impermeable boundaries hereafter.

How to obtain a symmetric positive-definite matrix $\boldsymbol{M}_i$ is the key step for the MFD method. A strict theorem is presented by Brezzi et al. in [40], where they give a recipe for constructing $\boldsymbol{M}_i$. Recently, Lie et al. [42] have discussed the corresponding implementations and some specific properties of the MFD. In this work, the following inner product has been used

$$\boldsymbol{M}_i=\frac{1}{|\Omega_i|}\boldsymbol{X}_i\boldsymbol{K}_i^{-1}\boldsymbol{X}_i^{\mathrm{T}}+\frac{d|\Omega_i|}{6\mathrm{tr}(\boldsymbol{K}_i)}\boldsymbol{A}_i^{-1}\left(\boldsymbol{I}-\boldsymbol{Q}\boldsymbol{Q}^{\mathrm{T}}\right)\boldsymbol{A}_i^{-1}, \tag{3.5}$$

where $\boldsymbol{Q}$ is an orthonormal basis for the range of $\boldsymbol{A}_i^{-1}\boldsymbol{N}_i$, $\boldsymbol{A}_i$ is the diagonal matrix with A_{ii} the face area of the i-th face, d the space dimension, and $\boldsymbol{I}$ the identity with dimension m.

3.2 Discrete fracture-matrix system

Obviously, the Eqs. (3.1)-(3.5) are applicable for matrix and fractures. However, it is noted that the fractures' formulation is in a lower space-dimension. Thus, the linear systems for

matrix and fractures can be written as follows, respectively

$$\begin{bmatrix} \boldsymbol{B}_{\rm m} & -\boldsymbol{C}_{\rm m} & \boldsymbol{D}_{\rm m} \\ \boldsymbol{C}_{\rm m}^{\rm T} & 0 & 0 \\ \boldsymbol{D}_{\rm m}^{\rm T} & 0 & 0 \end{bmatrix} \begin{bmatrix} \boldsymbol{v}_{\rm m} \\ \boldsymbol{p}_{\rm m} \\ \boldsymbol{\pi}_{\rm m} \end{bmatrix} = \begin{bmatrix} \boldsymbol{g}_{\rm m} \\ \boldsymbol{q}_{\rm m} \\ 0 \end{bmatrix}, \tag{3.6}$$

$$\begin{bmatrix} \boldsymbol{B}_{\rm f} & -\boldsymbol{C}_{\rm f} & \boldsymbol{D}_{\rm f} \\ \boldsymbol{C}_{\rm f}^{\rm T} & 0 & 0 \\ \boldsymbol{D}_{\rm f}^{\rm T} & 0 & 0 \end{bmatrix} \begin{bmatrix} \boldsymbol{v}_{\rm f} \\ \boldsymbol{p}_{\rm f} \\ \boldsymbol{\pi}_{\rm f} \end{bmatrix} = \begin{bmatrix} \boldsymbol{g}_{\rm f} \\ \boldsymbol{q}_{\rm f} \\ 0 \end{bmatrix}, \tag{3.7}$$

where the subscripts m and f denote the matrix and fracture respectively.

For the fracture-matrix connections, we consider the hybrid grid as described in Section 2.2. In the hybrid grid, a fracture is consider as a lower-dimensional object as interior boundary, and the fracture cell usually represented as a face of a matrix cell. Obviously, the fracture-cell pressures $\boldsymbol{p}_{\rm f}$ are part of the matrix-face pressures $\boldsymbol{\pi}_{\rm m}$, as illustrated in Fig. 3. Thus, in the coupling linear system, only the matrix-face pressures $\boldsymbol{\pi}_{\rm m}$ are retained.

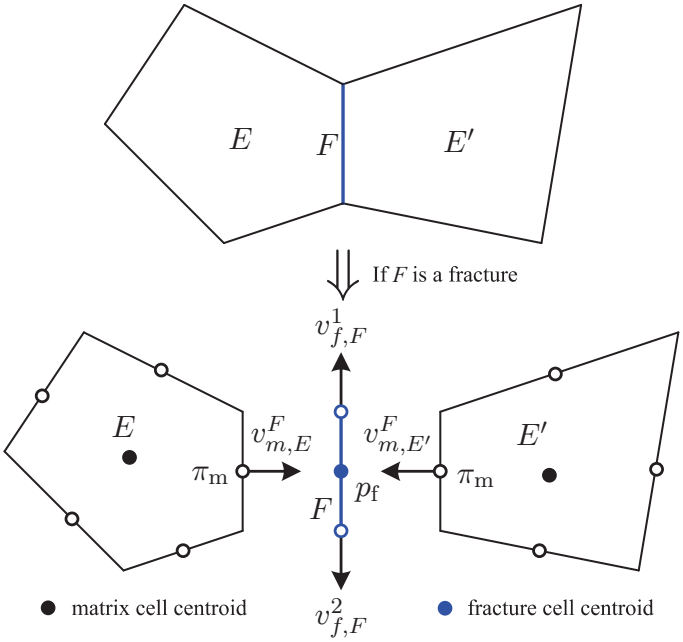

Figure 3: Schematic of combining the discretization in the matrix and fractures.

Simultaneously, the flux in Eq. (3.6) is written locally for all faces within each matrix cell. To link the cells in the mesh together, the following continuity conditions for the flux are imposed at each interface F of two neighboring cells E and E' ($F=E\bigcap E'$, see Fig. 3):

- If F is neither a fracture nor a barrier, the continuity of flux is imposed

$$v^F_{{\rm m},E}+v^F_{{\rm m},E'}=0. \tag{3.8}$$

- If F is a fracture, the total flux across both sides of the matrix-fracture interface defines the transfer function $Q_{\rm f}^F$ at F, which acts as a sink/source term for the fracture cell

$$\begin{cases} v_{{\rm m},E}^F + v_{{\rm m},E'}^F = Q_{\rm f}^F, \\ \sum v_{{\rm f},F} = Q_{\rm f}^F + q_{{\rm f},F}. \end{cases} \tag{3.9}$$

  Here, the second equation is the mass conservation in a fracture gridcell. And one should remember that the fracture's aperture a should be considered to calculate the flux of each fracture cell.

- If F is a barrier, the flux across F is zero, which can be imposed as a interior Neumann boundary condition in simple way.

Thus, the Eqs. (3.6) and (3.7) can be coupled through the matrix-fracture transfer function (Eq. (3.9)). And the resulting coupling linear system becomes

$$\begin{bmatrix} \boldsymbol{B}_{\rm m} & -\boldsymbol{C}_{\rm m} & \boldsymbol{D}_{\rm m} & 0 & 0 \\ \boldsymbol{C}_{\rm m}^{\rm T} & 0 & 0 & 0 & 0 \\ \boldsymbol{D}_{\rm m}^{\rm T} & 0 & 0 & -\boldsymbol{C}_{\rm f}^{\rm T} & 0 \\ 0 & 0 & -\boldsymbol{C}_{\rm f} & \boldsymbol{B}_{\rm f} & \boldsymbol{D}_{\rm f} \\ 0 & 0 & 0 & \boldsymbol{D}_{\rm f}^{\rm T} & 0 \end{bmatrix} \begin{bmatrix} \boldsymbol{v}_{\rm m} \\ \boldsymbol{p}_{\rm m} \\ \boldsymbol{\pi}_{\rm m} \\ \boldsymbol{v}_{\rm f} \\ \boldsymbol{\pi}_{\rm f} \end{bmatrix} = \begin{bmatrix} \boldsymbol{g}_{\rm m} \\ \boldsymbol{q}_{\rm m} \\ -\boldsymbol{q}_{\rm f} \\ \boldsymbol{g}_{\rm f} \\ 0 \end{bmatrix}. \tag{3.10}$$

There is no particular difficulty in constructing the above hybrid system. And it can be solved using a Schur-complement method and Aggregation-based Multigrid (AGMG) iterative method [46].

4 Discretization of the saturation equation

In this section, the FV discretization of the saturation equation is developed, which are valid for matrix and fracture gridcells. Only a short description of the method employed in this paper will be given. The interested reader is referred to [16, 43] for more details. And the upstream-weighting numerical scheme for multiple intersecting fractures is discussed in detail. In this work, the wetting phase is water, and the non-wetting phase is oil.

4.1 Upstream finite volume scheme

The saturation discretization in the i-th gridcell based on finite volume method is given as

$$\begin{aligned} &\int_{\Omega_i} \phi \frac{\partial S}{\partial t} \,{\rm d}\Omega + \int_{\partial\Omega_i} \left(f_{\rm w}(\boldsymbol{v} + \boldsymbol{K}\lambda_{\rm n} \cdot \nabla p_{\rm cnw} + \boldsymbol{K}\lambda_{\rm n} \cdot (\rho_{\rm w} - \rho_{\rm n})\boldsymbol{G}) \right) \cdot \boldsymbol{n}_i \,{\rm d}\Gamma \\ =& \int_{\Omega_i} q_{\rm w} \,{\rm d}\Omega. \end{aligned} \tag{4.1}$$

Here we dropped the subscript w for water saturation $S_{\rm w}$. Using the θ-rule for temporal discretization, a finite-volume scheme takes the following form

$$\frac{\phi_i}{\Delta t}(S_i^{k+1}-S_i^k)+\frac{1}{|\Omega_i|}\sum_{\gamma_{ij}}\Big(\theta F_{ij}(S^{k+1})+(1-\theta)F_{ij}(S^k)\Big)=q_{\rm w}(S_i^k), \tag{4.2}$$

where

$$F_{ij}(S)=\int_{\gamma_{ij}} f_{\rm w}(S)_{ij}(\boldsymbol{v}\cdot\boldsymbol{n}_{ij}+\boldsymbol{K}\lambda_{\rm n}\cdot\nabla p_{\rm cnw}\cdot\boldsymbol{n}_{ij}+\boldsymbol{K}\lambda_{\rm n}\cdot(\rho_{\rm w}-\rho_{\rm n})\boldsymbol{G}\cdot\boldsymbol{n}_{ij})\,{\rm d}\Gamma$$

is a numerical approximation of the flux over edge γ_{ij}. For a first-order scheme, it is common to use upstream weighting for the fractional flow

$$f_{\rm w}(S)_{ij}=\begin{cases} f_{\rm w}(S_i) & \text{if } \boldsymbol{v}\cdot\boldsymbol{n}_{ij}\geqslant 0,\\ f_{\rm w}(S_j) & \text{if } \boldsymbol{v}\cdot\boldsymbol{n}_{ij}<0. \end{cases} \tag{4.3}$$

In this work, an explicit scheme, i.e. θ=0, is employed. Such scheme is quite accurate but need impose stability restrictions on the time step, i.e. the CFL condition,

$$\Delta t\leqslant\frac{\phi_i|\Omega_i|}{v_i^{\rm in}\max\{f'_{\rm w}(S)\}_{0\leqslant S\leqslant 1}},$$

where

$$v_i^{\rm in}=\max(q_i,0)-\sum_{\gamma_{ij}}\min(v_{ij},0),\quad \frac{\partial f_{\rm w}}{\partial S}=\frac{\partial f_{\rm w}}{\partial S^*}\frac{\partial S^*}{\partial S}=\frac{1}{1-S_{\rm wc}-S_{\rm or}}\frac{\partial f_{\rm w}}{\partial S^*}.$$

Here S^* denotes the normalized water saturation.

4.2 Multiple intersecting fractures

We will use the generalization of the conventional two-point upstream-weighting technique to define the upstream-weighting in case of multiple intersecting fractures, which has been used successfully by Hoteit and Firoozabadi [23].

As depicted in Fig. 4, let I be the interface (line for 3-D domain and point for 2-D domain) connecting N_I fracture gridcells, e_i, $i=1,\cdots,N_I$. In each fracture gridcell e_i, the fractional flow function and the flux at I are denoted by $f_{{\rm w},e_i}$ and $v_{{\rm f},e_i}$. According to the signs of the fluxes, influx or efflux at I, we define an integer $0<n<N_I$, such that

$$\begin{cases} v_{{\rm f},e_i}\leqslant 0, & 0<i\leqslant n \quad \text{(efflux)},\\ v_{{\rm f},e_i}>0, & n<i<N_I \quad \text{(influx)}. \end{cases} \tag{4.4}$$

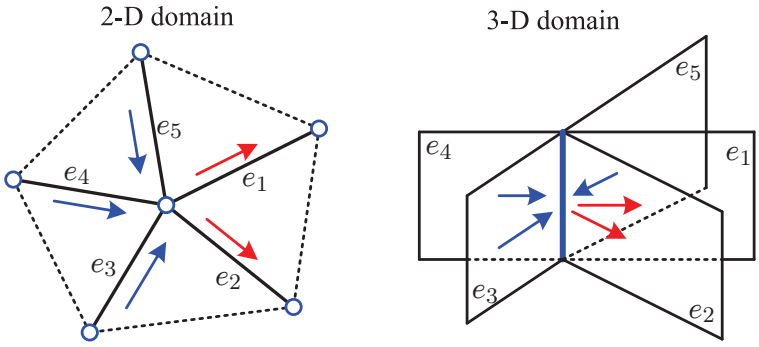

Figure 4: Grid with five intersecting fractures at I; the fractures e_1, e_2 are in the downstream, and e_3, e_4, e_5 are in the upstream.

By writing the total volumetric balance and the total mass balance at I, one gets

$$\sum_{i=n+1}^{N_I} v_{\mathrm{f},e_i} = -\sum_{i=1}^{n} v_{\mathrm{f},e_i}, \tag{4.5}$$

$$\sum_{i=n+1}^{N_I} f_{\mathrm{w},i} v_{\mathrm{f},e_i} = -\sum_{i=1}^{n} f_{\mathrm{w},I} v_{\mathrm{f},e_i} = -f_{\mathrm{w},I} \sum_{i=1}^{n} v_{\mathrm{f},e_i}. \tag{4.6}$$

And then, one can readily calculate the up-stream mobility for the effluxes at I, as follows

$$f_{\mathrm{w},I} = \frac{\sum_{i=n+1}^{N_I} f_{\mathrm{w},i} v_{\mathrm{f},e_i}}{\sum_{i=n+1}^{N_I} v_{\mathrm{f},e_i}}. \tag{4.7}$$

5 Numerical examples

To show the accuracy and applicability of the proposed method, four water-injection simulations are presented. We first consider a rock matrix with a single fracture to present the grid sensitivity of our numerical model. In the second case investigation, the robustness and the accuracy of the present algorithm are shown through a simple fractured block defined by horizontal and vertical fractures, which is derived from Ref. [34]. The third example shows the efficiency in numerical simulation of two-phase flow in 2D complex fractured porous media with fractures and barriers; and two different gridcell types also have been investigated to illustrate the grid flexibility of our proposed model. In the last example, the simulation results of a complex 3D discrete-fracture model have been shown.

5.1 Example 1: grid sensitivity

In order to examine the dependency of the size of the gridcells in our numerical model, we consider a 2D matrix block of dimensions 1 m $\times$ 1 m (x,y) with one fracture along the

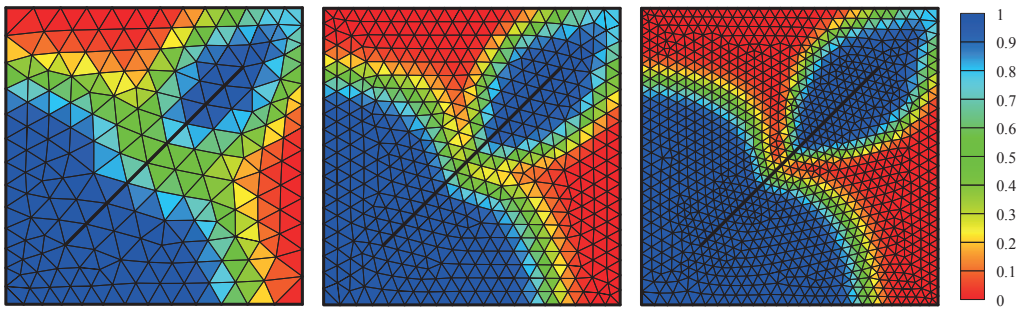

Figure 5: Water saturation profile after 1.5 PV water injection with different grid system. From left to right: 196, 479, 1096 grid nodes.

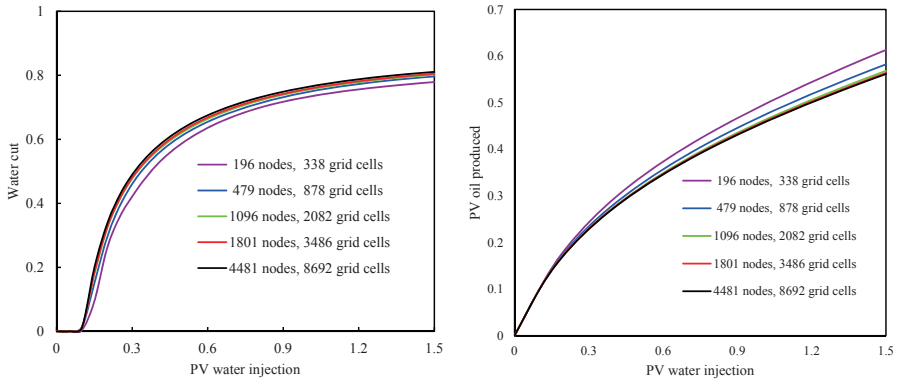

Figure 6: The curves of water cut and oil production vs. water injection during 1.5 PV water injection.

diagonal, as shown in Fig. 5. The endpoints of the fracture are located in $(0.2,0.2)$ and $(0.8,0.8)$, respectively. The whole domain is initially saturated with oil. We inject water at the bottom left corner, and the liquid is produced from the top right corner. The fluid and medium properties are provided in Table 1.

Water-flooding simulations are carried out for three different grid system. Due to the complexity of an unstructured grid, it is not easy to define an optimal grid. Herein, our purpose is only to obtain a grid good enough to allow the evaluation of the accuracy of the model. Fig. 5 presents the water saturation profile after 1.5 PV water injection. The history of oil production and water cut vs. water injection during 1.5 PV water injection is plotted in Fig. 6. And it has shown that the numerical results based on the grid system with 479 grid nodes is suitable for this example. This suggests us to do the subsequent simulations using the similar grid density as the grid system with 479 grid nodes.

5.2 Example 2: a simple fractured test model

To show the accuracy and efficiency of our numerical simulator, we consider a simple 2D fractured porous medium which is derived from ref. [34]. The geometry model includes

Table 1: Relevant data for Examples 1 and 2.

matrix properties: $\phi_m = 0.2$, $K_m = 1$ d ($\approx 0.9869 \times 10^{-12}$ m^2)
fracture properties: $\phi_f = 1.0$, $a = 0.1$ mm, $K_f = 8.33 \times 10^4$ d
fluid properties: $\mu_w = \mu_o = 1.0$ mPa·s, $\rho_w = \rho_o = 1000$ kg/m^3
residual saturations: S_{wc}=0.0, S_{or}=0.0
relative permeabilities: $k_{rw} = S_e$, $k_{ro} = 1 - S_e$, $S_e = \frac{1-S_w}{1-S_{wc}-S_{or}}$
capillary pressure: neglected
water injection and oil production rates: 0.01 PV/day

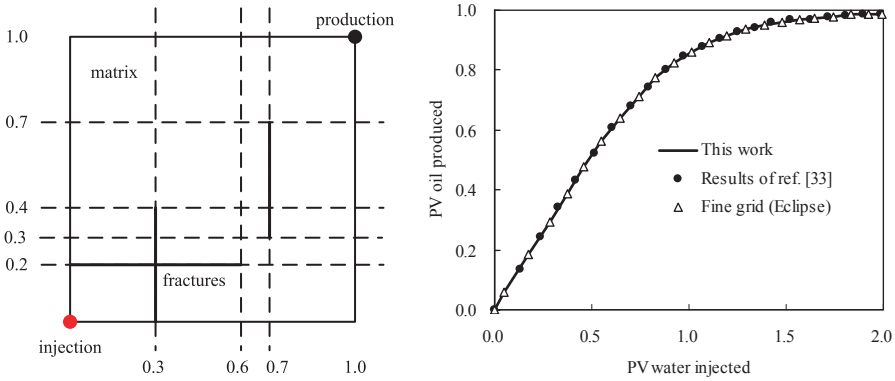

Figure 7: Sketch of geometrical of a simple 2D fractured porous medium (left); cumulative oil production curve (right).

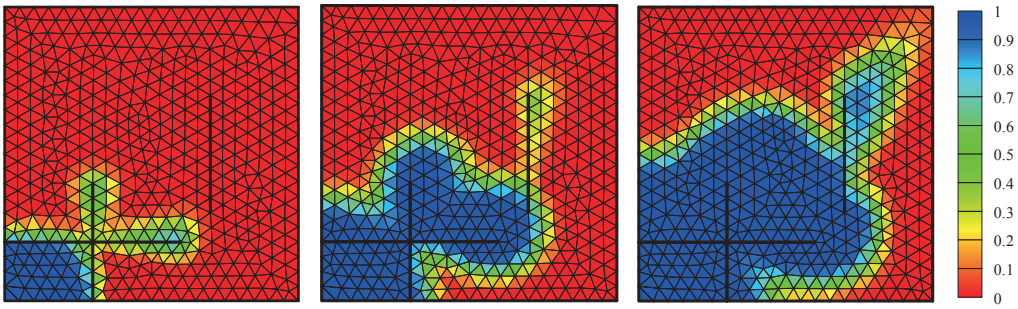

Figure 8: Water saturation profiles after 0.1, 0.3, and 0.5 PV water injected.

three fractures inside a domain, as depicted in Fig. 7. The relevant data are provided in Table 1 as same as Example 1.

Fig. 8 shows the water saturation profiles after 0.1, 0.3, and 0.5 PV water injected. The grid system contains 513 nodes, 946 matrix cells and 28 fracture cells. The excellent agreement between our present solutions and the results of Ref. [34] can be seen in Fig. 7, where we plot the cumulative oil production.

5.3 Example 3: 2D complex discrete-fracture model

In this example, we demonstrate the flexibility of the MFD method in modeling fractures and barriers. We consider a 2D rectangular domain initially saturated with oil, where several conductive fractures and a barrier are embedded in the porous medium, as illustrated in Fig. 9. The relevant data are provided in Table 2. Assuming that the reservoir model is water wetting, the capillary pressure curve follows Brooks-Corey capillary pressure function as shown in Eq. (5.1), and only the matrixs capillary pressure is considered.

$$p_c(S_w) = p_d \left(\frac{S_w - S_{wc}}{1 - S_{wc} - S_{or}} \right)^{-\frac{1}{\lambda}}, \quad 0.2 < \lambda < 3.0. \tag{5.1}$$

In order to show the applicability and efficiency of the proposed method, a fracture have been designed to intersect the barrier and crosses it (see Fig. 9), and two different gridcell types (triangle and quadrilateral) are used for the numerical simulations. The triangle grid system contains 881 grid nodes and 1615 gridcells, while the quadrilateral grid system includes 1859 nodes and 1737 gridcells.

Fig. 10 has shown the water saturation profiles at different time. The results indicate that the injected water displaces oil down the matrix and then moves forward rapidly along fracture when the oil/water front encounters conduit fractures. At the same time, the barrier forces the fluid flow along the extension direction of the barrier, as shown in Fig. 10. Evidently, the existence of fractures results in strong heterogeneity and anisotropy, which have a great influence on the fluid flow. Owing to the presence of capillary pressure, the oil recovery is improved due to the expansion of sweep area; however, the entire water-flooding effect is still controlled by the fractures.

Table 2: Relevant data for Example 3.

matrix properties: $\phi_m = 0.2$, $\boldsymbol{K}_m$ is the permeability tensor (see Fig. 9 for K_m^x)
fracture properties: $\phi_f = 1.0$, $a = 1$ mm, $K_f = 8.33 \times 10^4$ d
fluid properties: $\mu_w = 1.0$ mPa·s, $\mu_o = 5.0$ mPa·s, $\rho_w = \rho_o = 1000$ kg/m^3
residual saturations: S_{wc}=0.0, S_{or}=0.2
relative permeabilities: $k_{ro} = S_e^2$, $k_{rw} = (1 - S_e)^2$, $S_e = \frac{1 - S_w}{1 - S_{wc} - S_{or}}$
capillary pressure in fractures: neglected
capillary pressure in matrix: Brooks-Corey function (Eq. 21), p_d=1000 Pa, λ=1.0
water injection and oil production rates: 0.01 PV/day

5.4 Example 4: 3D complex discrete-fracture model

Here we consider a 3D fractured rock block of dimensions 100 m $\times$ 40 m $\times$ 16 m, $(x \times y \times z)$. The medium contains a filled fracture (red line) and several intersecting fractures (blue lines), as illustrated in Fig. 11. The injector is located at the left face of the block (i.e.

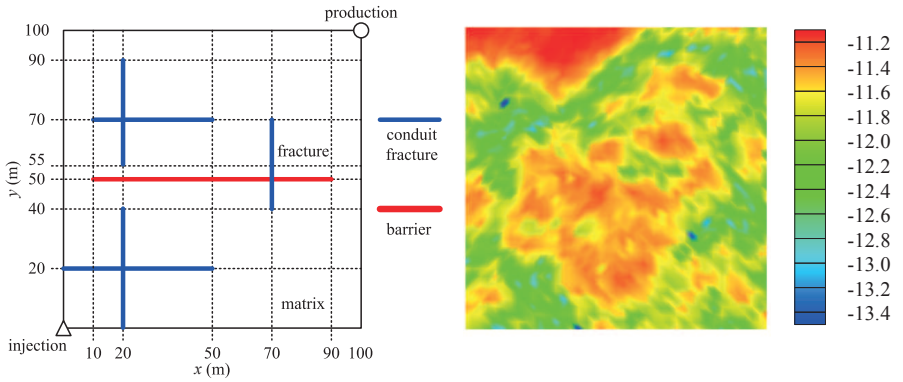

Figure 9: 2D fractured reservoir with complex fractures (left); the logarithmic permeability distribution of the matrix (right).

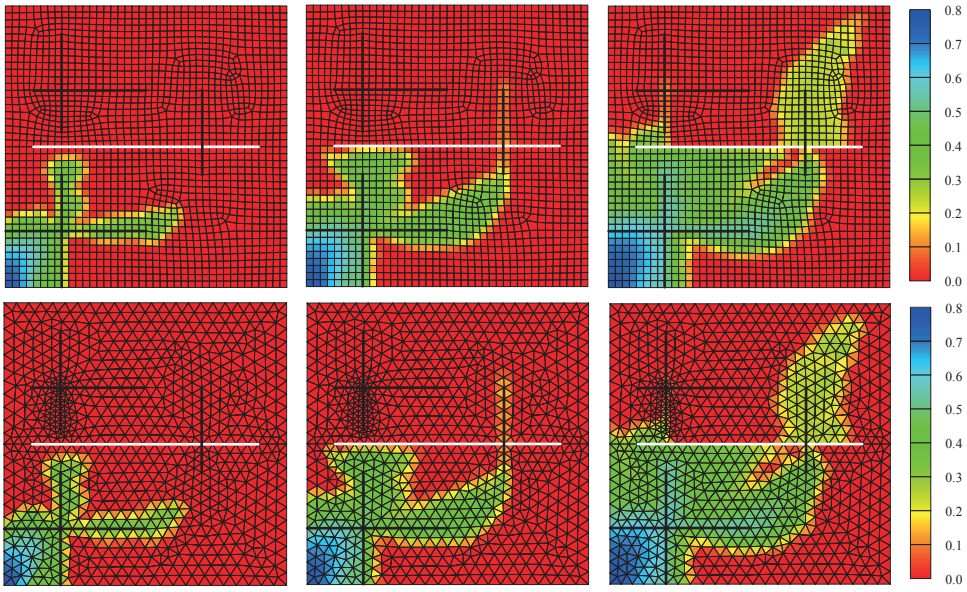

Figure 10: Water saturation profiles with two different gridcell types after 0.1, 0.2, and 0.4 PV water injected: quadrilateral gridcells (top), triangle gridcells (bottom).

at x=0 m) and the producer at the opposite right face (at x=100 m). The corresponding properties of the rock, fractures and relative permeability are provided in Table 3.

The domain is discretized into an unstructured mesh of 22124 matrix gridcells (tetrahedra) (see Fig. 11). In this example, the filled fracture is considered as a barrier. The corresponding water saturation profiles in the matrix and fractures are shown in Fig. 12. We would like to point out that the gridding for the present 3D discrete-fracture model is by no means optimal. In addition, all the four numerical tests were performed on a PC with 2.67 GHz Intel-Core i7 920 CPU and 8 GB of RAM.

Table 3: Relevant data for Example 4.

matrix properties: $\phi_m = 0.2$, K_m=1 md
fracture properties: $\phi_f = 1.0$, $a = 0.1$ mm, $K_f = 8.33 \times 10^5$ md
fluid properties: $\mu_w = 1.0$ mPa·s, $\mu_o = 1.0$ mPa·s, $\rho_w = \rho_o = 1000$ kg/m^3
residual saturations: S_{wc}=0.0, S_{or}=0.2
relative permeabilities: $k_{rw} = S_e$, $k_{ro} = 1 - S_e$, $S_e = \frac{1-S_w}{1-S_{wc}-S_{or}}$
capillary pressure and gravity: neglected
water injection and oil production rates: 0.001 PV/day

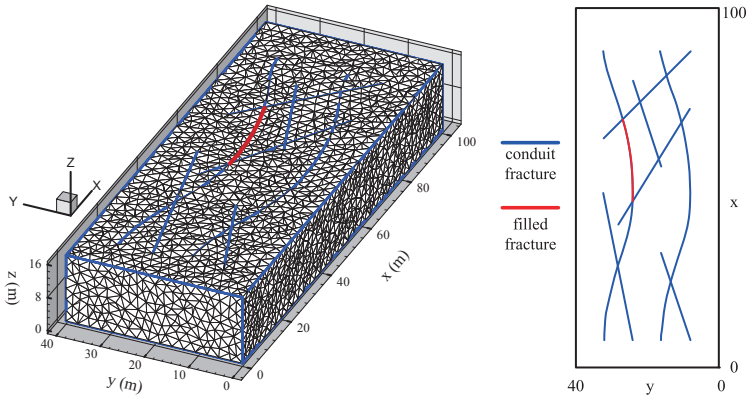

Figure 11: 3D discrete-fracture model with several conduit fractures and a filled fracture.

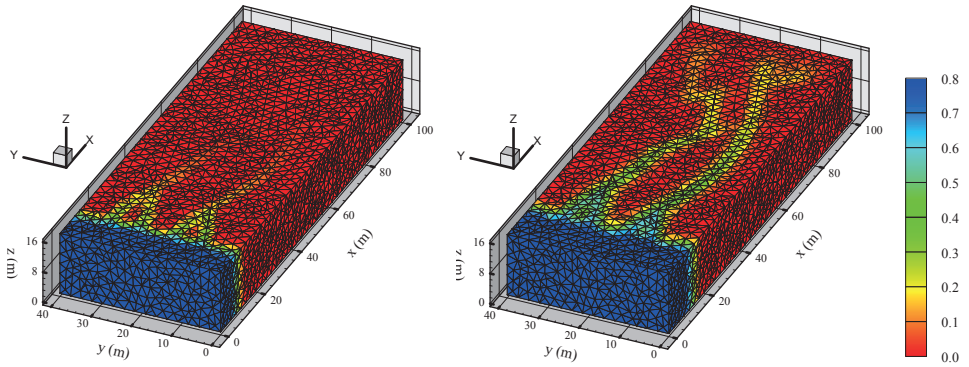

Figure 12: Water saturation profiles after 0.1 and 0.2 PV water injection.

6 Conclusions

The main features of this work can be summarized in three points:

1. A robust and efficient numerical approach has been developed for the two-phase flow simulation in discrete-fractured media. This numerical approach combines

the MFD and FV methods. The MFD method is used to approximate Darcys law, while the FV method is used to approximate the saturation equation. The numerical approach is applicable for both 2D and 3D discrete-fracture systems.

2. The MFD method provides a highly accurate approximation of the velocity field. The resulted formulation is similar to the mixed-hybrid formulation. However, the MFD approaches the discretization in a more easier way for general grids than MFE method, which resembles the conventional FD method. Therefore, our method is less mesh dependent than the conventional approximation, which have been illustrated through several examples. In the present numerical model, the flux through multiple intersecting fractures is accurately approximated in a natural way without any special assumption.

3. The discrete-fracture model is a powerful tool for fractured porous media. The geometrical simplification of the fractures significantly reduces the CPU and memory requirements. However, the gridding of complex fractured geological models is still a challenging issue, which deserves further research.

Acknowledgments

This work was supported by the National Basic Research Program of China (Grant No. 2011CB201004), the Important National Science and Technology Project of China (Grant No. 2011ZX05014-005-003HZ), the National Natural Science Foundation of China (Grant Nos. 11102237 and 51234007), and the Fundamental Research Funds for the Central Universities (13CX05007A, 13CX05017A, 14CX02042A).

References

[1] National-Research-Council-(US), Rock fractures and fluid flow: contemporary understanding and applications, National Academies Press, 1996.
[2] G. Barenblatt, I. Zheltov, I. Kochina, Basic concepts in the theory of seepage of homogeneous liquids in fissured rocks, J. Appl. Math. Mech, 24 (5) (1960) 1286–1303.
[3] J. Warren, P. Root, The behavior of naturally fractured reservoirs, Old SPE Journal, 3 (3) (1963) 245–255.
[4] H. Kazemi, A pressure transient analysis of naturally fractured reservoirs with uniform fracture distribution, Old SPE Journal, 9 (4) (1969) 451–462.
[5] H. Kazemi, K. Porterfield, P. Zeman, Numerical simulation of water-oil flow in naturally fractured reservoirs, Old SPE Journal, 16 (6) (1976) 317–326.
[6] T. Arbogast, J. Douglas Jr, U. Hornung, Derivation of the double porosity model of single phase flow via homogenization theory, SIAM Journal on Mathematical Analysis, 21 (4) (1990) 823–836.
[7] S. Geiger, M. Dentz, I. Neuweiler, A novel multi-rate dual-porosity model for improved simulation of fractured and multi-porosity reservoirs, in: SPE Reservoir Characterisation and Simulation Conference and Exhibition, SPE 148130, 2011, pp. 1–14.

[8] K. Lim, K. Aziz, Matrix-fracture transfer shape factors for dual-porosity simulators, Journal of Petroleum Science and Engineering, 13 (3) (1995) 169–178.
[9] P. Lemonnier, B. Bourbiaux, Simulation of naturally fractured reservoirs. state of the art. part 1 physical mechanisms and simulator formulation, Oil & Gas Science and Technology–Revue de lInstitut Français du Pétrole, 65 (2) (2010) 239–262.
[10] P. Lemonnier, B. Bourbiaux, Simulation of naturally fractured reservoirs. state of the art. part 2 matrix-fracture transfers and typical features of numerical studies, Oil & Gas Science and Technology–Revue de lInstitut Français du Pétrole, 65 (2) (2010) 263–286.
[11] K. Pruess, A practical method for modeling fluid and heat flow in fractured porous media, Old SPE Journal, 25 (1) (1985) 14–26.
[12] Y. Wu, K. Pruess, A multiple-porosity method for simulation of naturally fractured petroleum reservoirs, SPE Reservoir Engineering, 3 (1) (1988) 327–336.
[13] T. Narasimhan, K. Pruess, Minc: An approach for analyzing transport in strongly heterogeneous systems, in: E. Custodio, A. Gurgui, J. Ferreira (Eds.), Groundwater Flow and Quality Modelling, Springer Netherlands, 1988, pp. 375–391.
[14] Y. Wu, G. Qin, A generalized numerical approach for modeling multiphase flow and transport in fractured porous media, Communications in Computational Physics, 6 (1) (2009) 85.
[15] Y. Wu, C. Haukwa, G. Bodvarsson, A site-scale model for fluid and heat flow in the unsaturated zone of yucca mountain, nevada, Journal of Contaminant Hydrology, 38 (1) (1999) 185–215.
[16] Z. Huang, J. Yao, Y. Wang, An efficient numerical model for immiscible two-phase flow in fractured karst reservoirs, Communications in Computational Physics, 13 (2) (2013) 540–558.
[17] K. Ghorayeb, A. Firoozabadi, Numerical study of natural convection and diffusion in fractured porous media, SPE Journal, 5 (1) (2000) 12–20.
[18] S. Gebauer, L. Neunhäuserer, R. Kornhuber, S. Ochs, R. Hinkelmann, R. Helmig, Equidimensional modelling of flow and transport processes in fractured porous systems i, Developments in Water Science, 47 (2002) 335–342.
[19] L. Neunhäuserer, S. Gebauer, S. Ochs, R. Hinkelmann, R. Kornhuber, R. Helmig, Equidimensional modelling of flow and transport processes in fractured porous systems ii, Developments in Water Science, 47 (2002) 343–350.
[20] J. Noorishad, M. Mehran, An upstream finite element method for solution of transient transport equation in fractured porous media, Water Resources Research, 18 (3) (1982) 588–596.
[21] M. Karimi-Fard, A. Firoozabadi, Numerical simulation of water injection in fractured media using the discrete-fracture model and the galerkin method, SPE Reservoir Evaluation & Engineering, 6 (2) (2003) 117–126.
[22] V. Martin, J. Jaffré, J. Roberts, Modeling fractures and barriers as interfaces for flow in porous media, SIAM Journal on Scientific Computing, 26 (5) (2005) 1667–1691.
[23] H. Hoteit, A. Firoozabadi, An efficient numerical model for incompressible two-phase flow in fractured media, Advances in Water Resources, 31 (6) (2008) 891–905.
[24] S. Geiger-Boschung, S. Matthäi, J. Niessner, R. Helmig, Black-oil simulations for three-component, three-phase flow in fractured porous media, SPE Journal, 14 (2) (2009) 338–354.
[25] S. Lee, M. Lough, C. Jensen, Hierarchical modeling of flow in naturally fractured formations with multiple length scales, Water Resources Research, 37 (3) (2001) 443–455.
[26] A. Moinfar, W. Narr, M. Hui, B. Mallison, S. Lee, Comparison of discrete-fracture and dual-permeability models for multiphase flow in naturally fractured reservoirs, in: SPE Reservoir Simulation Symposium, SPE 142295, 2011, pp. 1–17.
[27] D. Carlo, A. Scotti, A mixed finite element method for darcy flow in fractured porous media

with non-matching grids, ESAIM: Mathematical Modelling and Numerical Analysis, 46 (02) (2012) 465–489.
[28] M. Karimi-Fard, B. Gong, L. Durlofsky, Generation of coarse-scale continuum flow models from detailed fracture characterizations, Water resources research, 42 (10) (2006) W10423.
[29] B. Gong, M. Karimi-Fard, L. Durlofsky, Upscaling discrete fracture characterizations to dual-porosity, dual-permeability models for efficient simulation of flow with strong gravitational effects, SPE Journal, 13 (1) (2008) 58–67.
[30] K. Slough, E. Sudicky, P. Forsyth, Grid refinement for modeling multiphase flow in discretely fractured porous media, Advances in water resources, 23 (3) (1999) 261–269.
[31] K. Slough, E. Sudicky, P. Forsyth, Numerical simulation of multiphase flow and phase partitioning in discretely fractured geologic media, Journal of contaminant hydrology, 40 (2) (1999) 107–136.
[32] S. Granet, P. Fabrie, P. Lemonnier, M. Quintard, A two-phase flow simulation of a fractured reservoir using a new fissure element method, Journal of Petroleum Science and Engineering, 32 (1) (2001) 35–52.
[33] J. Monteagudo, A. Firoozabadi, Control-volume method for numerical simulation of two-phase immiscible flow in two-and three-dimensional discrete-fractured media, Water resources research, 40 (7) (2004) W07405.
[34] M. Karimi-Fard, L. Durlofsky, K. Aziz, An efficient discrete-fracture model applicable for general-purpose reservoir simulators, SPE Journal, 9 (2) (2004) 227–236.
[35] T. Sandve, I. Berre, J. Nordbotten, An efficient multi-point flux approximation method for discrete fracture–matrix simulations, Journal of Computational Physics,.
[36] J. Kim, M. Deo, Finite element, discrete-fracture model for multiphase flow in porous media, AIChE Journal, 46 (6) (2000) 1120–1130.
[37] F. Brezzi, M. Fortin, Mixed and hybrid finite element methods, Springer-Verlag, Berlin, 1991.
[38] M. Wheeler, I. Yotov, A multipoint flux mixed finite element method, SIAM Journal on Numerical Analysis, 44 (5) (2006) 2082–2106.
[39] G. Singh, Mimetic finite difference method on gpu: application in reservoir simulation and well modeling, Ph.D. thesis, Norwegian University of Science and Technology (2010).
[40] F. Brezzi, K. Lipnikov, V. Simoncini, A family of mimetic finite difference methods on polygonal and polyhedral meshes, Mathematical Models and Methods in Applied Sciences, 15 (10) (2005) 1533–1551.
[41] F. Brezzi, K. Lipnikov, M. Shashkov, Convergence of the mimetic finite difference method for diffusion problems on polyhedral meshes, SIAM Journal on Numerical Analysis, 43 (5) (2005) 1872–1896.
[42] K. Lie, S. Krogstad, I. Ligaarden, J. Natvig, H. Nilsen, B. Skaflestad, Open-source matlab implementation of consistent discretisations on complex grids, Computational Geosciences, 16 (2) (2012) 297–322.
[43] J. Aarnes, T. Gimse, K. Lie, An introduction to the numerics of flow in porous media using matlab, Geometric Modelling, Numerical Simulation, and Optimization, (2007) 265–306.
[44] B. Niceno, Easymesh: a free two-dimensional quality mesh generator based on delaunay triangulation, `http://web.mit.edu/easymesh_v1.4`.
[45] H. Si, Tetgen: A quality tetrahedral mesh generator and a 3d delaunay triangulator, `http://tetgen.berlios.de`.
[46] Y. Notay, An aggregation-based algebraic multigrid method, Electronic Transactions on Numerical Analysis, 37 (6) (2010) 123–146.